Materials & Design 211 (2021) 110141

Contents lists available at ScienceDirect

Materials & Design

journal homepage: www.elsevier.com/locate/matdes

Superior fatigue endurance exempt from high processing cleanliness of Metal-Injection-Molded β Ti-Nb-Zr for bio-tolerant applications

Peng Xu [a,*], Florian Pyczak [b], Wolfgang Limberg [a], Regine Willumeit-Römer [a], Thomas Ebel [a,*]

[a] Institute of Metallic Biomaterials, Helmholtz-Zentrum Hereon, Max-Planck-Str. 1, D-21502 Geesthacht, Germany
[b] Institute of Materials Physics, Helmholtz-Zentrum Hereon, Max-Planck-Str. 1, D-21502 Geesthacht, Germany

HIGHLIGHTS

- Metal-Injection-Molded β Ti-Nb-Zr has superior fatigue endurance compared to clean-produced α-β Ti-counterparts while tolerating large contents of carbon and/or oxygen.
- The large amounts of oxygen and carbon do not facilitate crack initiation in "weak"-microstructural features/units of sintered metastable β Ti-alloys.
- Degraded fatigue property caused by coarse-grained microstructure might be mitigated or restrained by "fishbone"-like grain boundaries with rough multiphase interfaces.
- A conditional fatigue duality can be triggered by two competing mechanisms of crack initiation, initiating at α-platelets or at TiC-inclusions.

GRAPHICAL ABSTRACT

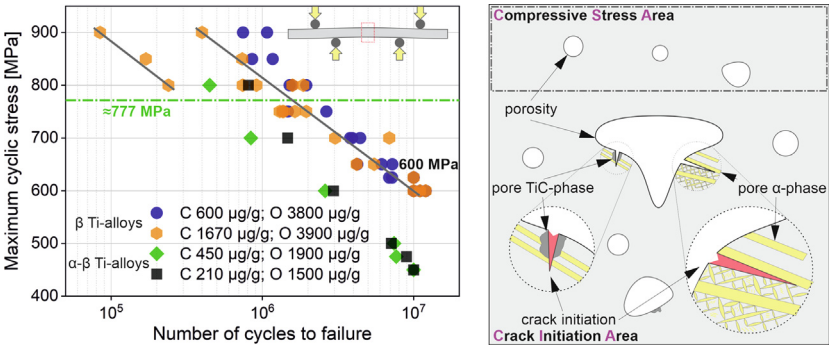

ARTICLE INFO

Article history:
Received 8 June 2021
Revised 27 September 2021
Accepted 30 September 2021
Available online 01 October 2021

Keywords:
Titanium alloy
Metal-Injection-Molding
Impurity
High cycle fatigue
Fracture mechanism

ABSTRACT

Technically optimizing the processing cleanliness of Metal-Injection-Molded titanium alloys (Ti-MIM) is not economically feasible. This problem is common in the materials processing field. In the search for an alternative approach, the work tries to achieve superior high-cycle fatigue (HCF) performance while tolerating very high impurity levels. The concept arose from the large tolerance of β-class Ti-alloys for oxygen-solutes and the feasibility to mitigate detrimental effects of carbide-inclusions, under monotonous loading. In this paper, MIM β Ti-Nb-Zr biomaterials for fatigue-critical applications were deliberately produced with very high O-level and normal/very high C-levels. The impurity-resistant Ti-biomaterials exhibit superior HCF endurance limits beyond 600 MPa irrespective of processing cleanliness, being significantly higher than those of the α-β Ti-reference alloys produced with tight restrictions on impurity levels. This superior fatigue performance while tolerating amounts of impurities stems from the "weak"-microstructural features insensitive to impurities and increased resistance of the Ti-matrix against fatigue small-cracks. Furthermore, a conditional fatigue duality triggered by two competing mechanisms of crack initiation in certain cases, initiating at microscale pore α-platelets and at large pore TiC-inclusions can occur. The success of the present alloy-process development might greatly relax the processing demands for active metals.

* Corresponding authors.
E-mail addresses: peng.xu@hereon.de (P. Xu), thomas.ebel@hereon.de (T. Ebel).

https://doi.org/10.1016/j.matdes.2021.110141
0264-1275/

1. Introduction

Historically, the field of material engineering has long resorted to more robust and advanced technologies to improve processing cleanliness or reduce impurity uptake. However, little work has been done to develop key structural materials robust against very high impurity levels. Theoretically, the mechanical property of active materials insensitive to impurities is capable of intrinsically overcoming low-cost and high-performance trade-off. In particular, this is economically important for some commercial processing technologies where the cost-effectiveness is an essential element, such as Metal-Injection-Molding (MIM) [1].

Due to its advantages of high mechanical performance, mass production capability, ability to form sophisticated shapes, and cost-savings, MIM technology to date has been used in industrialized applications in TMT (technology, media, and telecom), automotive, medical fields and so forth [2]. With regards to processing cleanliness, carbon and oxygen uptakes that are typical impurities originate mostly from starting powder, binder decomposition, and sintering furnace; the resulting impurity content of sintered parts is so high that MIM in essence has low cleanliness [3]. Many existing technical precautions, *e.g.*, usage of pre-alloyed material, high-purity powder and argon, careful handling, high-vacuum sintering, hydrogen-charging burnout prior to sintering, and avoiding graphite-heaters in furnaces, may not be completely successful solutions for actual manufacturing industry in pursuit of maximum benefits. Therefore, the nature of MIM technology currently confines its commercialization to ferrous metals, *e.g.*, carbon steel, whereas great challenges still remain for impurity-vulnerable active metals such as Ti, Nb, Zr, etc.

Recently, a Ti-Nb-Zr system (incl. ternary and multivariant) has been endorsed as a promising β-class Ti-alloy for bio-tolerant/fatigue-critical orthopaedic applications [4]. In theory, properly stabilizing β-phase of Ti-alloys can steeply lower Young's moduli without sacrificing other biomechanical properties to a certain extent [5]. A low Young's modulus may avoid bone replacement failure caused by the stress-shielding effect [6]. Among transition-metals that can stabilize β-phase, only Nb, Zr, Ta, and Hf are verified to feature the highest biocompatibility through diverse *in vitro* and *in vivo* evaluations [7]. In addition, the very active elements Nb and Zr are inclined to form oxides over the course of material service; but it has been verified that self-formed Nb_2O_5 and ZrO_2 oxide films with good toughness and corrosion resistance on the outer surface are of great benefit for crack resistance in NaCl solution (*i.e.*, body fluid) [8].

The β Ti-Nb-Zr processed by MIM thus has a tremendous potential to meet biomedical needs. However, its existing problem, *i.e.*, high or very high impurity levels are introduced to sintered active metals [2], has to be addressed in view of industrial applicability (mainly cost-effectiveness and technical-feasibility). In this paper, in accordance with ASTM B348 Grade 1 and Grade 2, O-level (C-level) in Ti-alloys less than 2500 μg/g (800 μg/g) and greater than 1800 μg/g are regarded as high impurity level, while O-level (C-level) in Ti-alloys greater than 2500 μg/g (800 μg/g) are regarded as very high impurity level. It was currently found that, in terms of ductility that is of greatest concern, many β Ti-alloys can endure oxygen solutes much better than the α-β Ti-alloys, for instance, Ti-6Al-4V and Ti-6Al-7Nb, in mechanical testing under monotonous loading [9]. Specifically, the β Ti-alloy can tolerate extraordinary oxygen levels up to *ca.* 8000 μg/g while still providing a moderate ductility in tensile tests [10]. On the other hand, normal carbon uptake with tight restrictions, or even below 500 μg/g in some cases, for MIM-processed β Ti-alloys frequently hampers ductility by precipitation of unfavorable TiC-inclusions along the prior β grain boundary (GB) as a major existing form of carbon atoms [11]. Nevertheless, it is feasible to improve the elongation to fracture largely through adjusting the spatial distribution of TiCs by regulating its precipitation path [4].

Though these perceived shortcomings of MIM β Ti-alloys in monotonous loading conditions have been well-addressed, fatigue under cyclic-stress loading is responsible for approximately 90% of mechanical failures in service [12]. However, prior to this research, there had been few fatigue studies on sintered β Ti-alloys. In fact, since a study launched by United States Air Force Scientific Advisory Board in 1992 targeting HCF [13], a variety of Ti-alloys have been extensively tested for fatigue under different cyclic-loading schemes, in many cases with surface treatment [14]. Unfortunately, those studies only provide limited reference, because most of them investigated pore-free or even defect-free Ti-materials, normally with extra-low interstitials.

What's more, compared with ingot-metallurgical or additive manufactured Ti-alloys characterized with rapidly cooled microstructures, slow furnace-cooled microstructures in traditionally powder-metallurgical as-sintered specimens have relatively coarse equiaxed-grains/colonies [15]. Of particular significance in this regard is that the small-crack effects, which in principle govern classic smooth-bar stress/life (fatigue S/N scatter) are closely related to the maximum size of "weak"-microstructural features/units [16]. It should be noted, that naturally occurring cracks, but not artificially pre-notched ones in fatigue samples are of significance. Their sizes are comparable to: i) the dimension of the microstructural unit oriented for easy small-crack nucleation/-growth (a continuum limitation); ii) the extent of localized plasticity ahead of the crack-tip (a linear-elastic fracture mechanics limitation); and iii) the extent of effective crack closure/shielding behind of the crack-tip (a similitude limitation) [17]. Therefore, in view of microstructural morphology, it has been generally recognized that fine equiaxed grains or variously oriented platelets associated with reduced effective slip-band lengths are more HCF-resistant than coarse lamellar colonies concomitant with extended planar slip bands [18,19].

For accurate assessment, it is necessary to experiment by using exactly the same MIM-processing and fatigue-testing parameters as employed for MIM common α-β Ti-alloys as reference (incl. Ti-6Al-4V [20] and Ti-6Al-7Nb [21] for comparing fatigue properties). A standard shot-peening process is performed on MIM as-sintered parts to erase harsh surface-defects. Testing surface-treated specimens allows for the identification of explicit effects of inner microstructural features of the materials on HCF [22]. By using high-quality powders and optimized processes with tight restrictions to achieve low impurity levels, both reference Ti-materials offer fatigue endurance limits of approximately 450 MPa. In these cases, initial HCF crack/slip-planes are oriented parallel to the weak lamellar interfaces acting as the maximum operative slip bands, partially/completely across one lamella within a colony or jumping occasionally to adjacent lamellae [23]. Specifically, it has been discovered that the smooth slip-bands/crack-facets in fracture surface initially open up within α/β lamellar-interfaces across α colonies with sizes of ≈ 148 μm in MIM Ti-6Al-4V [20] and ≈ 97 μm in MIM Ti-6Al-7Nb [21], when exactly the same processing and testing conditions were used. In contrast to MIM α-β Ti-alloys, there are basically no colony-type lamellar-structures of alternating α- and β-phase nor any coarse-grained equiaxed single-phase structure with geometrically flat GBs to provide operative dislocation slip-bands in most MIM metastable β Ti-alloys [24]. However, they have packets of small-sized α-platelets with various and often preferential orientations, precipitating initially at prior β grain boundaries and subsequently inside the β grains as a rule [25]. Interestingly, such inherently precipitated α-platelets with various orientations in the Ti-matrix conform materially to the HCF-resistant microstructures suggested

by Ritchie *et al.*, where "weak"-microstructural features are randomly oriented and size-minimized [26]. It naturally can: i) reduce operative slip-bands/crack-facets size by interrupting by intragranular α-platelets, which fairly rises cyclic stress threshold [26]; and ii) compel crack-tilt and -twist by randomly oriented slip/crack-planes, which effectively retards HCF crack propagation or even arrests the fatal/critical crack [27].

The work is to develop impurity-resistant active materials with superior fatigue endurance limits so that this material class can cater to low processing cleanliness technologies. Ti-MIM, as a typical example, always suffers from (very) high amounts of impurity uptake. The traditional strategies by technical-precaution/process-optimization to avoid impurities were abandoned here. A biotolerant MIM metastable β Ti-Nb-Zr material was studied, with the advantages of large tolerance to oxygen solutes and a certain feasibility to mitigate detrimental effects of carbide inclusions. In this study, the specimens were produced with deliberately introduced (very) high amounts of impurities. The impurities were mostly added by the following processes: blended powders method and conventional vacuum-sintering but altered sintering-cleanliness by either i) directly using dirty furnace or ii) running burnout prior to sintering, and shot-peening finishing; which caused either i) very high O- and C-levels in polluted-sintered Ti-parts or ii) very high O-level and normal C-levels in clean-sintered Ti-parts. The polluting sources were taken from a low-cost starting material and a dirty furnace without any burnout program, thereby imitating a bad production environment, other than adding carbon- and oxygen-containing powders. In the end, the impurity uptakes under the two different pathways, microstructures, and biomechanical properties of MIM Ti-Nb-Zr active materials for fatigue-critical applications are systematically characterized. Its fatigue crack resistance mechanisms, accounting for superior high-cycle fatigue properties in spite of very high carbon and oxygen concentrations, are elaborated. Moreover, the competing mechanisms of crack initiation giving rise to a conditional fatigue duality response and the propagation mechanism are illustrated. Furthermore, this work fills the lack of fatigue studies for powder metallurgical β Ti-alloys. This early study on the mechanisms of superior fatigue endurance insensitive to high amounts of impurities is likely a potent supplement to the efforts to overcome the low-cost and high-performance trade-off.

2. Method

2.1. Materials processing

The nominal composition of the metastable β-class Ti-alloy investigated in this study is Ti-20Nb-10Zr (units in wt.%, in the following text just referred to as Ti-Nb-Zr). Ti elemental powder (TLS Technik, Bitterfeld, Germany), Ti-42Nb master-alloyed powder (H. C. Starck, Goslar, Germany) and Zr elemental powder (Alfa Aesar, Haverhill, United States) were employed as the starting materials by the blended elemental/master-alloyed method. Other details of the raw powders are given in **Figure S1** in the file of **Supplementary Material**.

The feedstock of Ti-MIM consisting of the alloy composition proportioned metallic powders (powder packing ratio of *ca.* 67 vol%) and a common binder system [4] was sufficiently kneaded at a constant temperature of 120 °C for 4 hr under argon atmosphere for achieving homogeneous injection molding, through a mixer (Femix Misch- und Knettechnik, Waiblingen, Germany). After granulating, the feedstock was moulded into numerous green-parts with two geometric configurations for i) tensile testing [22] and ii) fatigue testing [20], via an injection-molding machine (Arburg, Lossburg, Germany). Specifically, the green-parts used for tensile testing are dog bone geometry (ISO 2740) with a length of 90 mm, while the others for fatigue testing are rectangular shape within a dimension of 50 mm × 6.3 mm × 3.4 mm.

Next after trimming the burrs, the green-parts were immersed in n-hexane (VWR CHEMICALS, Radnor, United States) within a debinding device (LÖMI, Grossostheim, Germany) at 40 °C for 15 hr. Subsequently, these (brown-)parts were placed in a vacuum furnace (XERION, Freiberg, Germany) and subjected to the conventional thermal debinding (isobaric argon flow at 5 mbar under 600 °C) and high vacuum sintering (at 10^{-5} mbar and 1500 °C for 4 hr with a set cooling rate of 10 °C min^{-1}) processes [4]. Note well this sintering cycle was run independently to produce two groups/batches of specimens varying in the sintering-pollution level, depending on the cleanliness of the vacuum sintering. One batch of Ti-parts was produced after performing a burnout cleanup program charging an argon/hydrogen gas mixture and defined as i) clean sintering. Another sintering cycle with a batch of Ti-parts was performed after heavy use of the furnace (around ten batches of Ti-MIM) without any burnout cleanup in-between them, defined as ii) polluted sintering, modelling bad production conditions.

At the end, shot-peening, as a widely accepted finishing technique for MIM-parts, was applied to as-sintered Ti-Nb-Zr parts of fatigue testing. Through adequate exposure under the bombardment of ZrO_2 shots with an average diameter of 0.5 mm, the surface-defects were obliterated/flattened and a hardening effect was remained in the surface layer [28].

2.2. Mechanical tests

Uniaxial tensile tests of clean-sintered MIM Ti-Nb-Zr were conducted on a servo-hydraulic structural test machine (Schenck-Trebel, Deer Park, United States), which is modernized with an electronic testing control (Zwick Roell, München, Germany) and equipped with a non-contact laser extensometer (Fiedler Optoelektronik, Lützen, Germany). Its tensile properties were determined for three specimens under standard manufacturing quality control at a strain rate of 0.5 mm min^{-1} at room temperature.

High-cycle fatigue tests of two batches of MIM Ti-Nb-Zr were performed on a resonant four-point bending machine (RUMUL, Neuhausen am Rheinfall, Switzerland). The default testing frequency was 95 Hz, the load ratio of minimum stress to maximum stress was set 0.2, and the stress was loaded in a sinusoidal line. The peak stresses ranged from 550 MPa to 900 MPa. The fatigue properties at each critical peak stress were repeated two to three times, whereas, near threshold value of critical stress for fatigue duality response behaviors, the fatigue properties were verified five times.

2.3. Materials characterization

In situ high-energy X-ray diffraction capable of characterizing trace phases (*e.g.*, TiC-phase with 0.55 area %) in high precision was performed at the Helmholtz-Zentrum Hereon operated HEMS beamline of Deutsches Elektronen-Synchrotron (DESY). This synchrotron radiation beam has a photon energy of 87.1 keV matching to a wavelength of 0.14235 Å. The diffractograms of Debye-Scherrer diffraction rings was recorded by using a PerkinElmer XRD 1622 flat panel detector. The cylindrical specimen (Ø 4.5 mm × 10 mm) that was cut from the MIM Ti-Nb-Zr part for tensile testing beforehand was measured in transmission.

Oxygen and carbon levels of all powders as well as of the clean- and polluted-sintered MIM Ti-Nb-Zr parts were determined for three specimens each by elemental analysis instrumentation (ONH836 and CS744 model) (LECO Corporation, St. Joseph, United States). The two batches of MIM Ti-Nb-Zr parts were prepared for

metallography via cutting, mounting, grinding, and polishing, before mechanical tests and (partially) after fatigue failures.

Optical microscope (Olympus Corporation, Tokyo, Japan) and scanning electron microscopes (Carl Zeiss AG, Jena, Germany; TESCAN, Brno, Czech Republic) were used to characterize: i) the morphology of starting powder (using SEM-SE mode, Secondary-Electron), ii) the clean- and polluted-sintered microstructures (using OM and SEM-BSE, Backscattered-Electron), iii) β grain size (using EBSD, Electron Backscatter Diffraction), iv) orientation relationships among different phases (using EBSD), v) fatigue fracture fractography (using SEM-SE), and vi) fatigue fracture profile (using SEM-BSE), respectively.

The average values (AVG) for the whole material of porosity and pore characteristics were determined on the basis of five optical microscopy images by ImageJ analysis software. Additionally, the holistic porosity was again calculated according to density measurement by Archimedes' principle determined for five fatigue specimens, to validate the accuracy of the performed image analysis. The local porosity and pore geometric characteristics of specific areas (incl. crack initiation area and crack propagation area) were calculated by ImageJ as well, which were determined for at least five scanning electron microscopy images of fatigue-failed parts respectively. The area fractions of TiC-inclusions in clean- and polluted-sintered MIM Ti-Nb-Zr parts were also calculated by ImageJ, determined for five optical microscopy images each.

3. Results and discussions

3.1. Composition, microstructure and mechanical properties

3.1.1. Porosity parameters and impurity uptake

The investigated MIM β Ti-Nb-Zr biomaterial exhibits general processing-drawbacks [29]; consequently, basic porosity structural parameters and grain size as well as alloy density are listed in Table 1, while its as-sintered impurity levels are given in Table 2. Compared with the earlier studies [30], these porosity parameters have been greatly improved, through optimizing the particle size/shape of partial starting powders as well as the tap density of blended starting powders. An example of this is the pore shape factor consequently rose from 0.64 to 0.77, where 1 denotes the circle. Apart from that, the residual porosity of *ca.* 3% in this Ti-Nb-Zr is essentially within the same level as that of the reference alloys, incl. Ti-6Al-4V and Ti-6Al-7Nb, in hereinafter fatigue-performance comparison. This is also a usual value in the accepted porosity range (*i.e.*, 1%−5%) of PM Ti-alloys [31].

These affordable Ti-42Nb and Zr powders used justifiably contain relatively high amounts of impurities, as detailed in **Figure S1**. Their oxygen levels are in the range of 3000–5000 μg/g. As a result, the impurity levels in as-sintered parts obtained are also very high, at least 1000–2000 μg/g higher than those of most reported PM-Ti alloys, as preliminarily defined very high impurities here. Specifically, the oxygen level of ≈ 3800 μg/g is about twice as high as those of the reference materials (*i.e.*, *ca.* 1900 μg/g in Ti-6Al-4V and *ca.* 1500 μg/g in Ti-6Al-7Nb) in this study, whereas the carbon concentrations of ≈ 600 μg/g in clean-sintered case and ≈ 1670 μg/g in polluted-sintered case are much higher than those (*ca.* 450 μg/g and 210 μg/g, respectively). In terms of sources of impurity uptake in conventional MIM technology, oxygen primarily stems from starting materials, whereas carbon is mainly picked up from debinding-sintering furnaces [4]. In this study, the nitrogen uptake in Ti-MIM simply from processing pollution is valued as negligible, being less than 240 μg/g even under polluted sintering.

3.1.2. Phase constitution and microstructure

The phase constitution and basic microstructure of as-sintered MIM β Ti-Nb-Zr biomaterial are displayed in Fig. 1. The ratio of α-phase to β-phase is approximately 50:50 deduced by *in situ* high-energy X-ray diffraction, where Nb and Zr could be major β-stabilizers in this alloy [32]. TiC-inclusions (The amount of 0.55 area % is a normal value under the circumstances of clean sintering) distribute in alignment along the β grain boundaries. Such an intermediate phase and its distribution pattern are common in most PM β-class Ti-alloys, but not usual in the common α-β Ti-counterparts [11]. A more detailed evolutionary mechanism of TiC precipitation can be found in a previous report [4]. Electron backscatter diffraction (EBSD) shows the existence of large-sized β-grains, in which intragranular 2D-acicular α-phase and porosity are uniformly and randomly dispersed (see Fig. 1**c**). Compared with as-sintered Ti-6Al-4V with a mean grain/colony size of approximately 100 μm but prepared by the pre-alloyed method in the literature [1] and the reference materials herein, the grain size in this Ti-Nb-Zr alloy is almost three times as high (see also Table 1). Owing to the use of blended starting powders, the sintering process being compelled at a very high temperature for the sake of homogeneity is a reason of strong grain growth [33].

Fig. 2 reveals that substantial microscale and nanoscale 2D-acicular α-phase regions were uniformly precipitated in the form of hierarchical dispersion inside β-grains. Differing from colony-structures of alternating α- and β-phase, they exhibit a three-dimensional "tent"-architecture that appears as a pyramid with each of its faces composed of a α-variant. Inspection of a variety of β-grains of the Ti-Nb-Zr using EBSD (set probing step-size: 0.5 μm) demonstrates that in terms of microscale α-phase (excl. nanoscale α-phase), in all cases only 8 α-variants of the theoretical possible 12 α-variants according to the Burgers orientation relationship nucleate from a single parent β-grain, rather than all 12 α-variants. The α-variant preferential selection-behavior and dual-scale "tent"-stuctural α-platelets here are in line with the lit-

Table 1
Alloy density, grain size, and structural parameters of porosity.

Sintered density [g/cm^3]	(β) Grain size [μm]	Porosity [unitless]	Average pore diameter [μm]	Pore shape factor [unitless]
5.01 ± 0.01 (gauged) 5.15 (theoretical)	293 ± 24	2.7% ± 0.3% (by imaging) 2.7% ± 0.1% (by Archimedes)	7.3 ± 5.6	0.77 ± 0.19

Table 2
Impurity levels and TiC area fraction in MIM Ti-Nb-Zr produced by changed sintering-pollution degrees via burnout cleanup and heavy usage of sintering furnace.

Sintering cleanliness	Carbon [μg/g]	Oxygen [μg/g]	Nitrogen [μg/g]	TiC area fraction [area %]
Clean	597 ± 53	3775 ± 6	188 ± 11	0.55 ± 0.06
Polluted	1670 ± 51	3893 ± 49	235 ± 3	2.14 ± 0.25

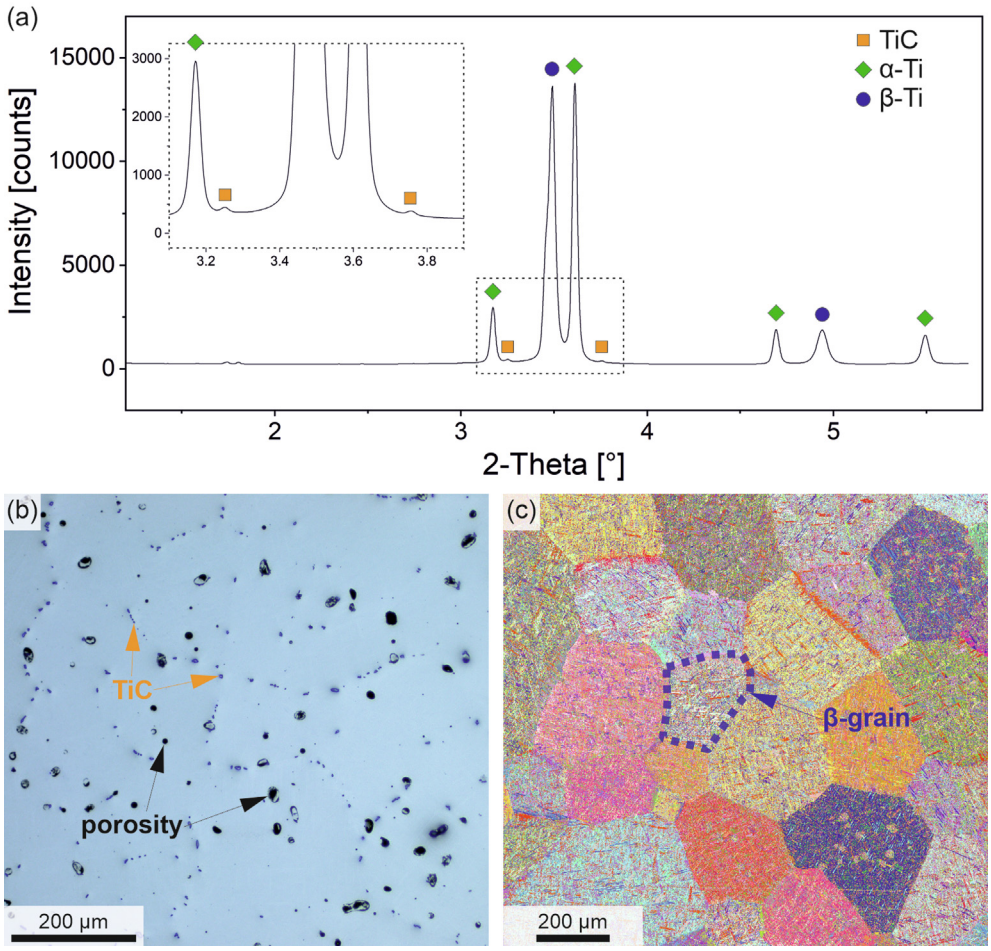

Fig. 1. Phase constitution and basic microstructure of MIM β Ti-Nb-Zr biomaterial produced by clean sintering. (a) High energy XRD pattern indicating the presence of only α-, β-, and a trace amount of TiC-phase; (b) OM image showing dispersed pores and aligned TiCs; and (c) EBSD figure exhibiting large-sized β-grains.

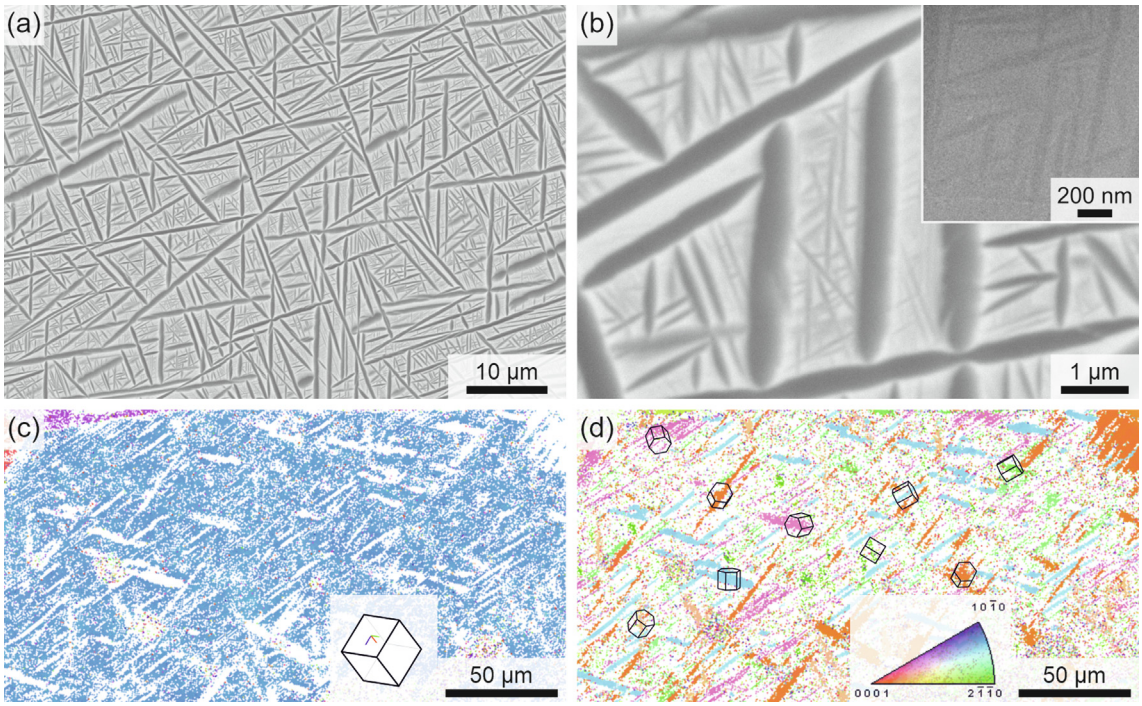

Fig. 2. Microstructure of β-grains. (a) SEM-BSE image at lower magnification, where the dark phase is α-phase while the bright phase is β-phase; (b) SEM images at higher magnifications demonstrating there are micro- and nano-scale α-phase within 3D "tent"-architecture; (c) EBSD figure of β-phase in a typical β-grain; and (d) a variety of lattice orientation (selection preference of α-variants) of its inner microscale α-phase.

erature [25]. Especially for slowly cooled PM Ti-alloys, the variant selection is more pronounced governed by dislocation driving than by chemical driving [25].

Relatively long grain boundaries (GBs) of MIM Ti-Nb-Zr are usually decorated with GB α-precipitates and GB TiC-inclusions, as can be seen in Fig. 3; their formation is related to GB-regions enriched with impurities [34]. In fact, a so-called single TiC-particle with widely recognized elongated-shape [35] in PM β-class Ti-alloys is often assembled from a plurality of TiC-particles with irregular shape, indicated in Fig. 3**b**. On the other hand, the GB α-precipitates as a whole frequently present a typical "fishbone"-like morphology, and evidence for this is shown in Fig. 3**c**. Furthermore, these side-plates of a certain GB α-phase, in essence, belong to distinct crystallographic α-variants in the different spatial directions inside adjacent β-grains, and therefore are in most cases more or less misoriented against each other [24]. In most cases, the backbone of the GB α-phase has an identical orientation with one of the side-plates of a GB α-phase but within the same GB α-phase this can occasionally alternate so that some sections are crystallographically oriented to the side plates on one and other sections parallel to the side plates on the other side [36]. This is the reason why such a grain boundary even if appearing straight in lower magnification is winding on a micron level. From now on, such a GB containing GB α-phase will be termed an absolute grain boundary. It is defined as the exact interface between two GB α-variants featuring a slight lattice misorientation. Analogous absolute GBs like this, which are actually winding on a micron level, have also been found in other β-class Ti-alloy [37] and β-solutionized α-β Ti-alloy [38]. Compared with those flat absolute GBs on a micron level, these winding absolute GBs may have significantly different effects on crack initiation and propagation.

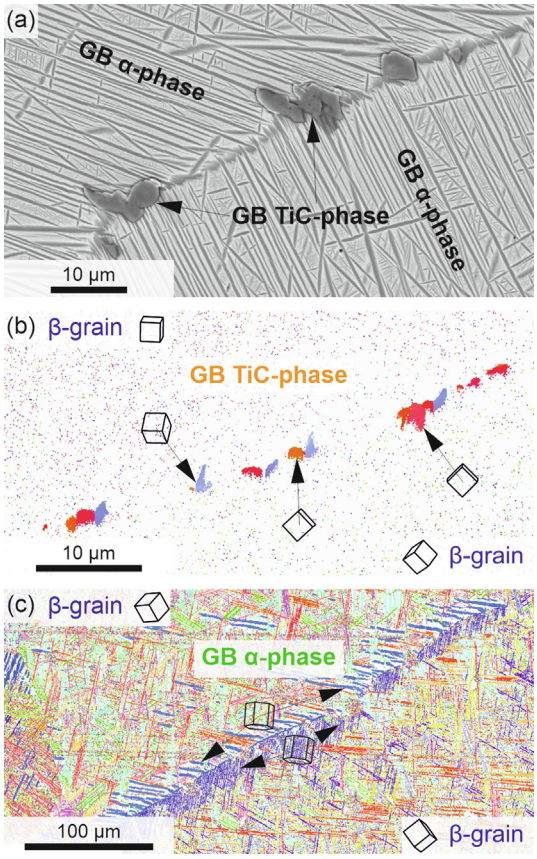

Fig. 3. Structure, phase constitution, and orientation relations among these phases at grain boundaries (GBs). (a) The "fishbone"-like GB α-phase, in which TiC-phase is occasionally embedded; (b) EBSD figure manifesting that elongated TiC-phase might be composed of multiple delicate TiC-individuals (*i.e.*, a plurality of TiCs); and (c) a slight misorientation between side-plates of "fishbone"-like GB α-phase.

3.1.3. Tensile and fatigue properties

3.1.3.1. Tensile properties. The room-temperature tensile testing results of MIM Ti-Nb-Zr are given in **Table S1**, and the engineering stress–strain curves are plotted in **Figure S2** in the file of **Supplementary Material**. Merely tensile properties of conventionally clean-sintered parts are presented, as materials failure under monotonous loading is not the core issue in this paper. For tensile studies on this type of alloy, please refer to the previous publication [4]. A Young's modulus of 74 GPa is lower than that of most metallic biomaterials [39]. Secondly, elongation to fracture upwards of 6.5% is also sufficient for the intended application and remarkably high, considering that this material contains an oxygen level as high as approximately 3800 μg/g. Note that, unlike common α-β Ti-alloys (*e.g.*, a critical value of *ca.* 3300 μg/g in Ti-6Al-4V [9]) particularly susceptible to oxygen solutes and not apparently to carbon, the ductility of β-class Ti-alloys has appreciably high oxygen tolerance [10], but is rather vulnerable to excessive amounts of carbon [11].

Tensile strength does not always correlate with fatigue strength, nevertheless a higher static bearing-strength obtained in fatigue-critical structural materials can often support a relatively higher maximum for the fatigue endurance limit. In this regard, the beneficial reinforcement of the Ti-matrix of MIM Ti-Nb-Zr can be ascribed to the high concentration of solute elements including Nb, Zr, O, etc. [40], as well as to hierarchical dual-scale (incl. microscale and nanoscale) intragranular α-precipitates with the "tent"-architecture in high density. In contrast, very large grain size (*ca.* 293 μm) and residual porosity of about 3% are two major drawbacks on bearing-strength. With regard to (GB-)TiC dispersoids, although they are often added as stiff reinforcing particles in some light alloys (*e.g.*, magnesium alloys [41]), so far the effectiveness of carbon-deficient TiC_x (x less than 1) with lower fracture strengths during tensile loading as strengthening precipitates in Ti-alloys is still ill-defined [42].

3.1.3.2. Fatigue properties. In Fig. 4 high-cycle fatigue (HCF) properties among β Ti-Nb-Zr biomaterial and common α-β Ti-reference alloys are compared, where all materials were produced by essentially the same i) MIM-processing, ii) conventional clean vacuum-sintering, and iii) shot-peening finishing. Since the polluted sinter-

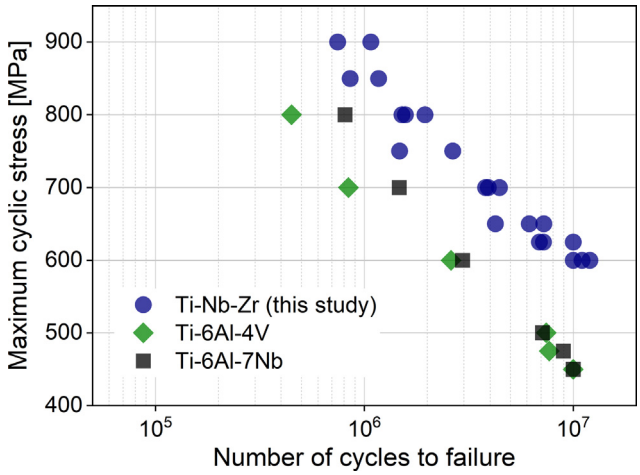

Fig. 4. High-cycle fatigue (HCF) properties of MIM β Ti-Nb-Zr biomaterial produced by clean sintering, compared with MIM α-β Ti-reference alloys. Please note corresponding four-point bending fatigue testing parameters used in all materials herein were exactly the same and all points at 10^7 cycles were run-outs.

ing can induce the investigated biomaterial to have a fatigue duality behavior, its particular fatigue failure mechanism will be illustrated separately in **Section 3.3**. Notwithstanding the presence of ductility-unfavorable TiC-inclusions and very high O-levels, this Ti-Nb-Zr material has an excellent fatigue endurance limit (cyclic stress at 10^7 cycles) of 600 MPa, in contrast to 450 MPa in both reference materials, which all were processed by MIM. This is also the first time the fatigue performance of PM β-class Ti-alloys has been reported. The mechanism of microstructural resistance to fatigue crack initiation and propagation that enables this Ti-material to possess superior fatigue performance exempt from high processing cleanliness is elaborated in the next two sections.

Interestingly, from the perspective of impurity levels, the effects of oxygen uptake on the fatigue behaviors of different classes of Ti-alloys are contradictory when considering the available studies. Bache *et al.* [43] claimed that fatigue crack propagation could be accelerated when Ti-6Al-4V contains internal oxygen concentration in excess of 1700–2300 μg/g. Hidalgo *et al.* [44] discovered that the rise of interstitial oxygen levels significantly degraded the fatigue endurance limit for Ti-6Al-7Nb. Moreover, it has been demonstrated that the increase of oxygen content caused the reduction of fatigue strength and/or lifespan in unalloyed-Ti [45] and Ti-6Al-2Sn-4Zr-2Mo [46]. On the contrary, Liu *et al.* [47], Li *et al.* [8], Long *et al.* [48] and Cho *et al.* [49] indicated that oxygen additions enhance the fatigue endurance limits of β-class Ti-alloys, through enhancing the resistance to the fatigue crack initiation/propagation, *e.g.*, by grain refinement induced by oxygen atoms. Furthermore, there was no practically adverse influence of oxygen content on fatigue crack growth in some β-class Ti-alloys either [50].

However, there is no report regarding the effects of carbon on fatigue behavior of Ti-alloys yet. It seems logical that for most (α-β) Ti-alloys that have higher carbon solubility (*i.e.*, the cases where carbon atoms fully dissolve into Ti-matrix), carbon is likely to impair fatigue properties in the form of partial oxygen equivalent. Conversely, for many β-class Ti-alloys, besides dissolved carbon atoms also TiC-precipitates are present. These carbide-inclusions will certainly have a different impact on fatigue behavior compared to carbon atoms in solution. As a result, its influences on the type of competing fatigue small-crack initiation mechanisms taking place in as-sintered β-class Ti-alloys are illustrated in **Section 3.2** and **Section 3.3**.

3.2. High-cycle fatigue failure mechanism

Examination of all broken parts reveals that there are three distinct areas in the fracture surface in all cases. Typical examples for MIM Ti-Nb-Zr are given in Fig. 5. In the subsurface layer, a small "crater"-like area with winding ridges radiating from the center (*i.e.*, so-called "fish-eye" crack) is identified as the crack initiation area (CIA), marked by an orange dotted circle. The top surface of the bent beams was subjected to the highest tension during four-point bending fatigue testing. Apart from CIA, the remaining two areas have different roughness and are separated by a white line. The relatively even terrain filled with tearing ridges, starting from the "crater" of the CIA, is the crack propagation area (CPA). The other area is the unstable fracture area (UFA), where several bare grains or pits remaining from missing grains (*i.e.*, grains being on the matching other fracture surface) can be found. However, some studies have stated that more than one crack may take place in fatigue failure process, even the fatal crack might not be the one initiated first [51]. In the case presented here, no other cracks were discovered on the side surfaces of the broken fatigue parts. This implies that even if there were multiple small-cracks initiated, those nonlethal-cracks did not grow sufficiently to reach the outer surface or were completely arrested, then being dormant, which might be attributable to strong crack-stoppers by diverse shielding effects [52].

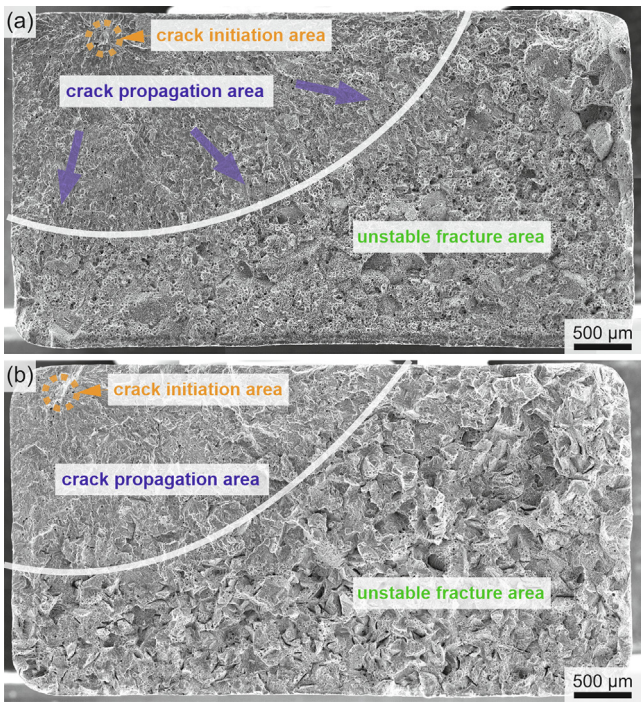

Fig. 5. The topography of typical fracture surface of HCF failure of the MIM Ti-Nb-Zr produced by (a) clean sintering and (b) polluted sintering.

3.2.1. Fatigue crack initiation mechanism

The classical model of metal fatigue has been well-established, that is under cyclic stress loading the to-and-fro slip movement of the dislocation slip-bands can generate extrusions and intrusions at the surface, thereby initiating the fatigue small-crack [53]. It is reported that the cyclic stress intensity factor (ΔK) is unsuited to describe the microstructural small-crack regime [54] and it is more precise to consider a critical stress, rather than a stress intensity, for naturally occurring cracks [26]. Nevertheless, stress intensity factor (ΔK) theoretically pertains a corresponding large-crack regime, *e.g.*, a pre-crack created artificially by removing the crack wake. Moreover, the growing rate of a small-crack is far in excess of the corresponding large-crack subjected to an equally applied driving force [23]. Following Mott [55] and Stroh [56], the critical stress of fatigue crack initiation, $\Delta\tau_c$, can be formulated as Equation (1):

$$\Delta\tau_c = 12\alpha G/n \tag{1}$$

where α is equal to $\gamma/(\boldsymbol{b}G)$, γ represents the surface energy, $\boldsymbol{b}$ is the Burgers vector, G denotes the shear modulus, and n is the amount of planar dislocation pile-ups. Given n is greatly related to the operative slip-band length, it is conceivable that a long dislocation slip-band bordering on a free surface is a "soft spot" [57], as initial fatigue small-crack may centre on the preferential nucleation site [26]. With regard to the Ti-alloys that contain lamellar microstructural features of α-platelets or α-colonies, these weak-bonded phase interfaces or grain boundaries in-between hcp-lattice α-phase and bcc-lattice β-phase are most likely to be the preferential operative slip-bands or crack-facets for fatigue crack nucleation [58]. In addition, it is well-known that the crack initiation site can be shifted from the outer surface to the subsurface by surface treatment processes. The shot-peening process has the ability to significantly harden the near-surface layer being able to

shift the crack initiation location underneath the peened layer. One example is the creation of a compressive stress area (CSA) to depths ranging up to *ca.* 100 μm in a Ti-Al alloy [28].

The representative fractograph indicating the CIAs of clean-sintered MIM Ti-Nb-Zr can be seen in Fig. 6, and a more detailed example is visible in **Figure S3** in the **Supplementary Material**. A rather large-sized or an irregular-shaped pore can be always found in the center of the "crater" with a cleavage facet bordering on the porosity-wall. Based on the studies via three-dimensional phase-field simulations [25], the shapes of the smooth cleavage facets (see **Figure S3a**) correspond to the geometry of microscale α-phase and certainly not to nanoscale α-phase or other phases in this case. In terms of microstructural lengths, i) TiC-phase has an average particle-diameter of 6.6 μm [4], ii) nanoscale α-phase is merely submicron long, iii) microscale α-phase in geometric length direction often reach tens of microns capable of providing the longest planar crystallographic slip band, and iv) prior β grains with micro-winding absolute GBs, not flat interfaces, hardly offer effective slip bands, although average grain size is up to 293 μm. A factor of note, in most metals, is that the geometry of GBs could decide whether they can provide effective slip-bands or crack-planes [27]. The porosity-walls in the near-surface area functioning similar to a free surface facilitate the dislocation slip-bands to reciprocate without structural restrictions under cyclic stress loading, while the operative slip bands might stem from microscale α-phase with the longest weak-bonded interfaces. Hence, it is evident that the studies completed here are in good agreement with the aforementioned theories.

Unlike as-cast or hot-worked cases, the investigated β Ti-Nb-Zr processed by MIM or other traditional PM technologies is a typically pore-containing material. In nature, a porosity-wall acts as a free surface for dislocation slip-bands and a stress concentration raiser during fatigue loading, which accordingly has a strong impact on fatigue behaviors. Thus, it is imperative to investigate in detail the implications of pores in the CIA for fatigue failure of MIM Ti-Nb-Zr. In order to characterize the local porosity structural parameters in the territory of the "crater" a designated CIA in this investigation can be defined such that this area is a circle with a radius of 100 μm centered on the particular pore which has initiated the crack. The results of porosity structural parameters of the designated CIA in comparison to the situation in the unfatigued alloy on a comparable area called average area (AVG; for numbers see Table 1) are plotted in Fig. 6**b**–**d**, calculated using the method described in **Section 2** and in the earlier report [30]. By evaluating these parameters, it is clear that there are severely pore-related defects in the CIAs, especially average pore diameter and porosity in the CIA deviate by up to about four times from the average values based on the holistic porosity.

3.2.2. Cyclic stress-induced crack stable propagation mechanism

The fatigue fracture-surface and -profile of the CPA of MIM Ti-Nb-Zr produced by clean sintering are presented in Fig. 7. In order to gain greater insight into the role of porosity on fatigue, a comprehensive comparison is provided in Fig. 7**c**–**e**. The first impression from the histograms is that the porosity structural parameters in the CPA are between those of AVG and the worst-case CIA. In effect, on closer examination, the fatigue crack path seems to be preferentially located in areas with relatively high porosity (*i.e.*, a small bearing cross-sectional area) as can be seen from Fig. 7**d**, instead of areas with a single larger and/or more irregular pore similar to the case in the CIAs.

Microcracks with a length of *ca.* 10 μm can be found in Fig. 7**a**. By fracture profile analyses these microcracks appearing in the fracture surface are actually identified as branches of fatal cracks (*i.e.*, crack bifurcation behavior, not extended secondary crack). These cracking bifurcation and deflection in the fatal crack paths appear to be caused by microscale α-phase, as indicated in Fig. 7**b**. Furthermore, most crack segments of the fatal crack paths are oriented along the phase-interfaces of microscale α-platelets, ascribed to a limited number of slip systems available within hcp α-lattice [16].

Firstly, crack bifurcation is also an effective crack preventer, due to needed extra energy for the fatal crack to branch [26]. It seems like the fatal crack paradoxically did not seek a rather easy path without superfluous damage energy consumption. The mechanism of crack bifurcation as a necessary byproduct of the crack locally propagating along a path of instantaneous low energy consumption is explained below. The 3D "tent"-architecture of α-phase spatially contains a great deal of twist and tilt weak-bonded slip/crack-plane misorientation [27] (neither purely lattice misorientation, nor previously misinterpreted 2D crack inclination [59]). A sufficiently large twist angle can cause retardation or even arrest of crack growth along these planes. The resumption of arrested cracks propagating across the twist and tilt slip/crack-plane misorientation can be effected by crack branching through reducing the twist and tilt angles and necessary tear lengths of strong-bonded sections [27]. This is also the reason why the crack branches open to a certain extent (see Fig. 7**b**). When the fatal crack crosses the misorientation junction of the slip/crack-planes having sufficient twist and tilt angles, a superfluous extended weak-bonded section of slip/crack-planes is fractured in exchange

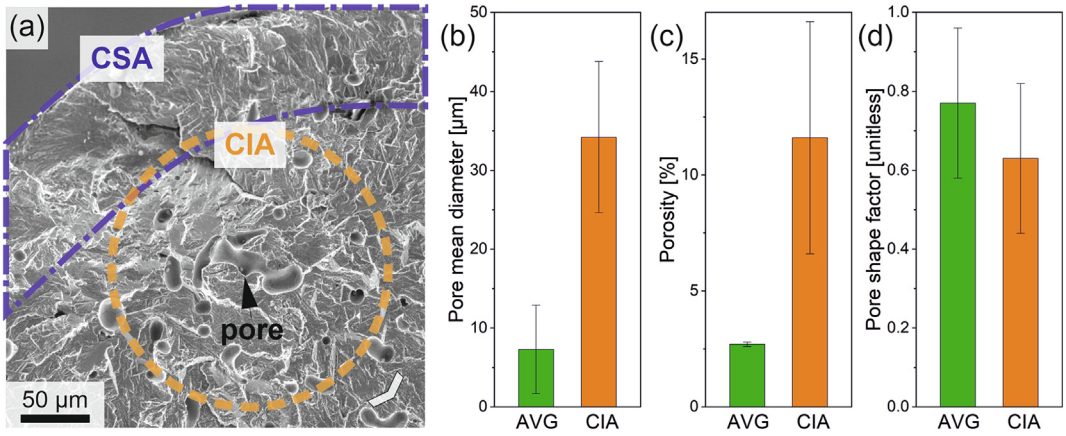

Fig. 6. (a) SEM-SE fractograph of crack initiation area (CIA) in the subsurface underneath compressive stress area (CSA) of the peened near-surface layer; and (b)–(d) the comparison of porosity structural parameters between the CIA and average area (AVG) of the whole material.

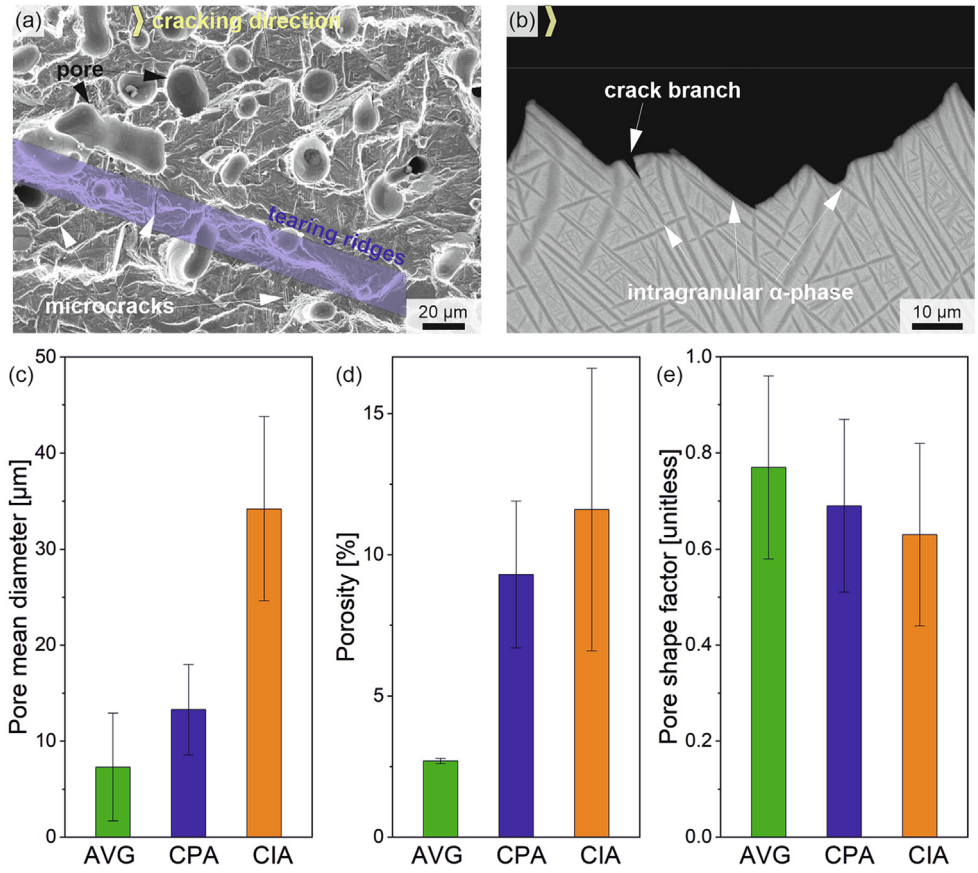

Fig. 7. (a) SEM-SE fractograph of crack propagation area (CPA); (b) SEM-BSE fracture profile of the CPA; and (c)–(e) comprehensive comparisons of these porosity structural parameters among AVG, CPA, and CIA.

for a smaller tearing-area of the strong-bonded structure, to achieve the lowest instantaneous energy consumption.

Secondly, the observed highly-serrated edge from the fracture-profiles of the CPA is mainly yielded by the crack deflection that is a well-documented crack-stopper [52]. The fatal cracks advance along "tent"-architectural microscale α-phase. In principle, its long α/β-interfaces with certain orientations enable the easiest cracking, just for instantaneous situations, but eventually formed serrated-like fracture edges. This effect and aforementioned bifurcation greatly increase the length and tortuosity of the crack path prior to final failure of the part. Apart from that, it is widely recognized the roughness-induced crack closure mechanism theoretically valid for large-crack growth produced by repetitively cracking along twist and tilt slip/crack-planes is mainly responsible for crack growth retardation [60]. It is worthy to mention that a higher average misorientation angle (incl. 3D twist and tilt angles) tends to cause larger crack deflection and consequent larger crack-growth retardation [61]. Therefore, it seems highly probable that increased misorientation caused by the inherent selection preference of α-variants for microscale α-phase in the present material (see **Section 3.1.2**) enhances fatigue large-crack growth resistance.

3.2.3. Strain-induced unstable fracture mechanism

As the fatal crack grows, the remaining effective bearing cross-section shrinks continuously. When the actual bearing stress ahead of the crack-tip exceeds the yield strength of 855 MPa in this Ti-Nb-Zr, complete failure will take place shortly after via strain-induced damage mode from the initial cyclic stress-induced damage mode. Theoretically, strain-induced fracture mechanisms at the end-stage of four-point bending fatigue, analogous to tensile fracture, of MIM Ti-Nb-Zr could follow i) the voids coalescence mode and ii) the cleavage fracture mode from the fracture behavior theory suggested by Ritchie [62]. Furthermore, a discussion in regard to the cracking evolution during plastic deformation in this Ti-Nb-Zr can refer to the publication [4]. In this paper, the fractography for the UFA is provided in Fig. 8, as a support and supplement to the previous studies.

The fractography of the UFA mainly contains two kinds of distinct topography, as shown in Fig. 8**a**. Firstly, there are a large number of pits representing pores acting as rather large voids surrounded by relatively deep dimples. This could indicate that the fatal cracking path occurred inside β-grains via i) void coalescence mode. The second is the standard cleavage plane with very shallow dimples and a small number of broken pores via ii) cleavage fracture mode. Cleavage fracture occurred at grain boundaries, where the geometry of the cleavage plane is consistent with the general curvature of GBs and coarse grain morphology [63]. Moreover, many TiC fragments are clearly identifiable in these cleavage planes (see Fig. 8**b**), which also agrees with the morphology of cleavage fracture previously observed by tensile-damaged Ti-Nb-Zr biomaterials [4].

The fracture-edge profile of cleavage planes is represented in Fig. 8**c**. It can be seen that cracks passed through the backbone of fishbone-like GB α-phase and GB TiC-phase. The winding crack paths on a micron level are virtually in line with the morphology of absolute grain boundaries observed by EBSD measurement in this study. The crack propagation paths inside β-grains are strongly influenced by the porosity-guided redirection, as evident from the Fig. 8**d**. An enlarged image (Fig. 8**e**) indicates that the redirection

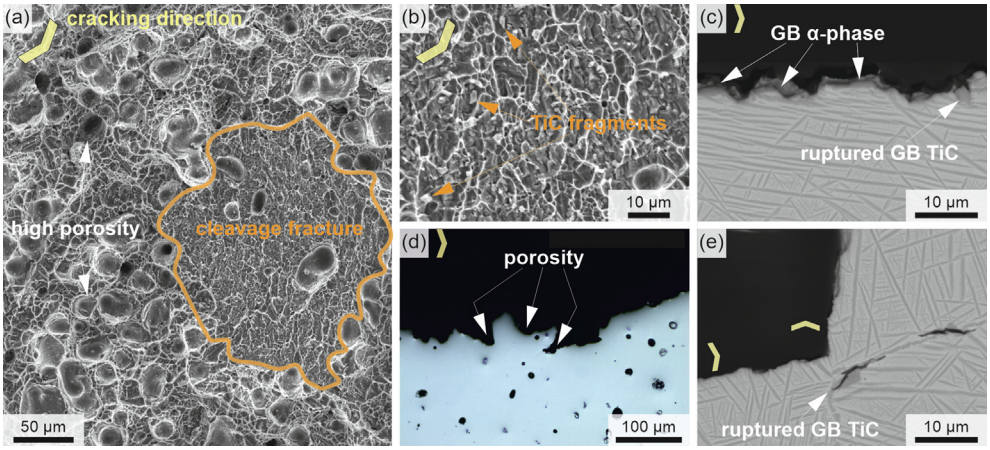

Fig. 8. Fractography of unstable fracture area (UFA). (a) UFA consists of many pits, cleavage planes and rather deep dimples; (b) shallow dimples and TiC fragments were found on the cleavage planes; (c) cracking along GBs; and (d)–(e) porosity-guided crack redirection, in spite of presence of ruptured TiCs alongside the fatal crack path.

action can even ignore the presence of ruptured TiCs near the front of the crack. Such ruptured TiCs out of the fatal crack paths were only found in the fracture subsurface of the partial section of UFA. Nevertheless, they cannot be discovered from either deeper region in the UFA or any depth region in the CPA. The results indicate that MIM Ti-Nb-Zr in the UFA in four-point bending fatigue did not undergo uniform deformation like that in the tensile tests, but merely elicits a localized plastic deformation zone ahead of crack-tips. The reason is that with the advancement of cracks, the region ahead of crack-tips underwent plastic deformation successively due to the decreasing effective bearing cross-section and the nature of stress gradient induced by four-point bending fatigue loading.

On the basis of the above observations and analyses, the high-cycle fatigue failure mechanisms of MIM metastable β Ti-Nb-Zr containing general sintered defects could be illustrated in Fig. 9.

3.3. Conditional duality of fatigue behavior under polluted sintering

In this section, we evaluate the high-cycle fatigue property of MIM Ti-Nb-Zr produced by polluted sintering. First, the analysis results of impurity uptake for polluted-sintered Ti-parts were listed in Table 2, together with values of clean-sintered specimens for comparison. These results suggest that changes in the cleanliness of the sintering process can significantly influence carbon uptake but has less effect on oxygen and nitrogen uptake. This likely attributes to carburization reactions, especially for the fine powder compact with a high specific surface area. There is heavy volatilization of carbon-containing matters at the high-temperature in the complex-configuration structured debinding-sintering furnaces, which is difficult to get clean [64]. It is important to note that this does not mean that oxygen uptake from the sintering atmosphere is negligible, but that did not fluctuate in line with the sintering cleanliness changed by the burnout cycle and heavy usage of sintering furnace. Besides, the area fraction of resultant TiC-inclusions has increased by a factor of approximately four, as evident from **Figure S3d**.

The HCF testing results of polluted-sintered Ti-Nb-Zr are shown in Fig. 10. Surprisingly, its fatigue endurance limit is not degraded even minimally under low sintering cleanliness, mainly excessive carbon uptake. Furthermore, below the dash-dot-line, the fatigue responses are retained irrespective of the sintering cleanliness, as can be seen from Fig. 10**a**. Interestingly, in the higher stress region, the fatigue lifespans of the polluted-sintered apparently scatter on two distinct trajectories. However, both are subpar marginally shifting to left as well, if the clean-sintered results are considered as a benchmark/criterion. It is generally acknowledged that the fatigue S-N curve of a metal is usually on a core trajectory with a small dispersion. However, such an unusual phenomenon, *i.e.*, fatigue responses appearing in proportion onto two trajectories, has been first discovered by Ravi Chandran in Ti-10V-2Fe-3Al alloy and was defined as fatigue duality [65]. It has been well-established that fatigue duality derives from the competing mechanisms between different categories of defects that can initiate fatigue cracks. Which crack initiation mechanism can prevail or be activated is highly dependent on the quantity, heterogeneity, geometric shape, effective size, spatial distribution, occurrence probability of the defect, and the synergy (*i.e.*, synergistic interaction) of defects in combination, etc. [65]. Later, similar phenomena have been observed in a variety of Ti-alloys, often seen in multi-defect containing materials processed by some specific technologies, such as powder metallurgy [66]. Nevertheless, a conditional fatigue duality is found and explained here for the first time. It means that the fatigue S-N curve changes from one core trajectory to two separated trajectories, when the loading peak stress increases beyond a threshold (*e.g.*, ≈ 777 MPa in the investigated MIM Ti-Nb-Zr), where another crack initiation mechanism can be activated.

The fracture surface (Fig. 5**b**) and topographic characteristics of the polluted-sintered specimens are comparable to those of the clean-sintered ones. The CIA topography on the core trajectory of S-N curves is represented in Fig. 10**b**, likewise comparing well with that of clean sintering. That is, locally worse porosity structural parameters in comparison to AVG promote the pore α-phase initiation of fatigue cracks by dislocation band slipping, as elaborated in **Section 3.2.1**. By contrast, examination of the CIAs on the condition-triggered trajectory reveals that fatigue cracks can be initiated despite the absence of excessive pores, as shown in Fig. 10**c**. Such a combination of a large-sized TiC and a normal porosity can be repeatedly observed on the "crater" (see **Figure S3b** at a higher magnification). It may be inferred that the dislocation pile-ups after accumulating to a certain extent could lead to stress concentration at the porosity-walls, which gives rise to cleavage fracture tearing TiC-phase when the actual stress on high-modulus TiCs exceeds their bearing strength via stress-transferring effect. The ruptured TiC-inclusions with a large size could replace the small-crack facets usually induced by microscale pore α-platelets and practically brought about the cleavage facets as initial cracks. As a result, the fatigue lifespan might be reduced by premature crack initiation and be accordingly scattered on the

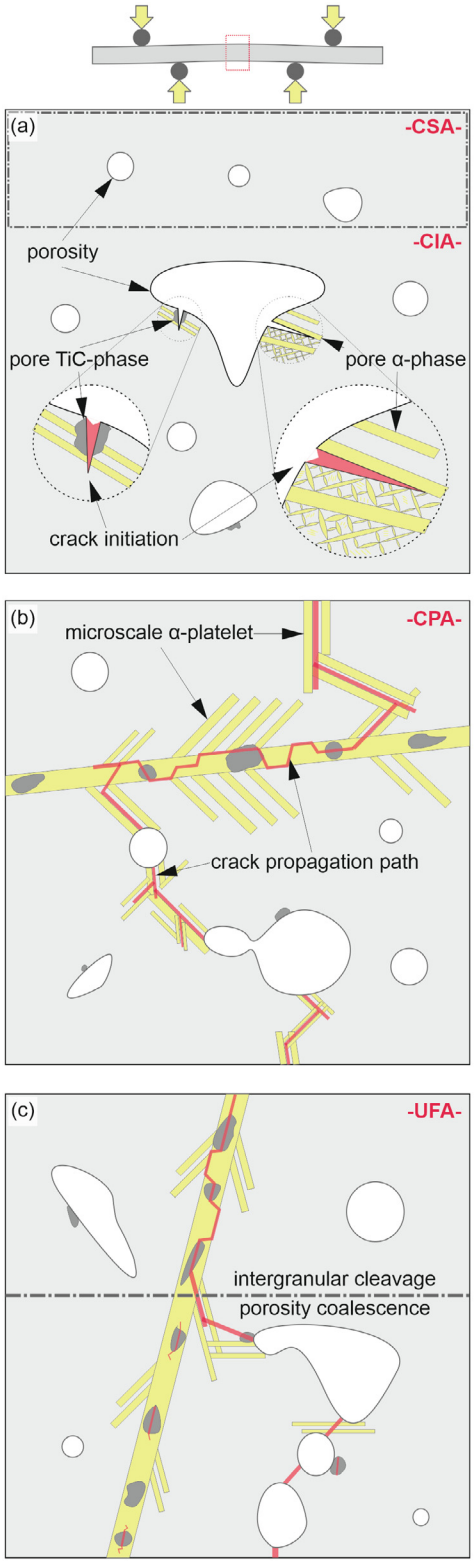

Four-point bending fatigue test setup
- min/max stress ratio of 0.2
- sinusoidal waveform
- frequency of 95 Hz

Compressive stress area (CSA)
- near surface layer
- true stress decreased by hardening treatment

Crack initiation area (CIA)
- at subsurface layer
- true stress increased by worse local porosity structural parameters

The competing mechanisms to initiate fatigue small-crack:
i) predominant irreversible dislocations slip/crack at microscale pore α-platelets interface

ii) alternative intragranular cleavage fracture of large pore TiC-particles merely over certain stress threshold after accumulating dislocation pile-ups

Crack propagation area (CPA)
- true stress below the yield strength

Stable crack propagation along the following microstructural features:

i) microscale α-platelets with various orientations to cause cracking deflections and bifurcations

ii) grain boundaries to possibly generate tearing ridges

iii) pores to reduce effective bearing cross-section area

iv) necessary β Ti-matrix to promote cracking, e.g., the junction of the crack-planes with twist and tilt angles

Unstable fracture area (UFA)
- true stress above the yield strength

Unstable crack tearing along the following microstructural features:

(via ordinal strain-induced fracture modes ahead of crack-tips in disregard of crack-stoppers)

i) "fishbone"-geometric grain boundaries with well-bonded delicate TiC-particles, via intergranular cleavage mode

ii) areas with locally worse porosity structural parameters, via porosity coalescence mode

Fig. 9. High-cycle fatigue failure mechanisms in as-sintered metastable MIM β Ti-Nb-Zr biomaterial containing typical powder metallurgical defects. Schematics of the uniform moment region between the loading inner rollers of a four-point bending fatigue test specimen.

second trajectory. A theoretical threshold value at *ca.* 777 MPa is the initial value of local stress concentration that was calculated, if mainly taking into account the AVG-porosity of 2.7%, overall yield strength of 855 MPa in MIM Ti-Nb-Zr and the localized CIA-porosity of 11.6%, when only these key factors were taken into consideration. Even this calculated value seems to be in good agreement with the experimental data.

Apart from these two competing major crack-initiation mechanisms described, a unique CIA topography was observed, as reported in Fig. 10**d**, of which an enlarged image is given in **Fig-**

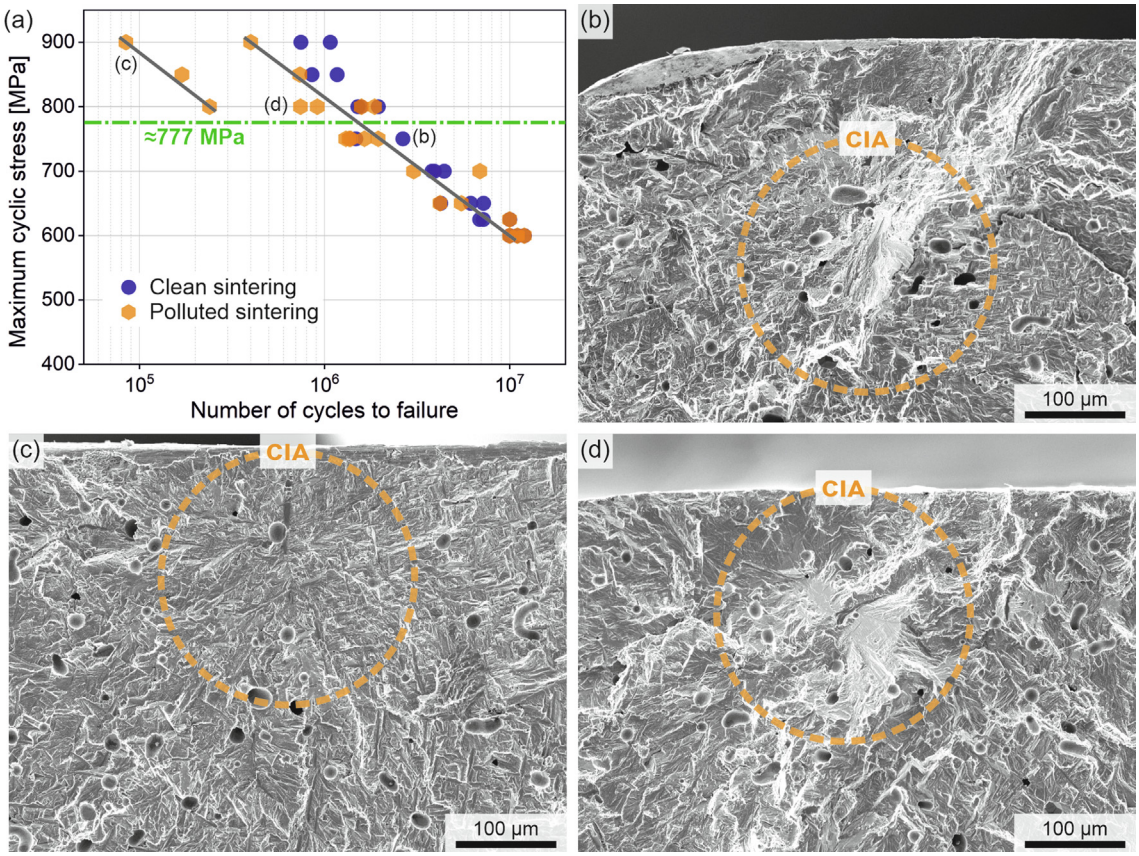

Fig. 10. (a) HCF of MIM Ti-Nb-Zr produced by polluted sintering; (b) the CIA topography of dominant crack initiation mechanism for relatively higher lives; (c) the CIA topography of a pore TiC inclusion initiating fatigue crack; and (d) an unique CIA topography triggered by the synergistic interaction.

ure S3c. The most striking features of this "crater" are the inclusion of a community of fishbone-like GB α-phase, a GB TiC-phase falls within the team of upper left fishbone-like GB, and moderate porosity. This fatigue crack initiation was occasionally caused by the synergistic interaction from such a rare combination but simultaneously was suppressed on account of the lack of an effective free-surface. In the end, the crack propagation mechanisms in the polluted-sintered can be referred to those of the clean-sintered elucidated in **Section 3.2**, since no apparent abnormalities were found, except that more and larger ruptured TiCs in cracking paths contribute to a reduction in fatigue lifespan, *i.e.*, marginally shifting to left.

4. Conclusions

A metastable β Ti-20Nb-10Zr material was designed for biotolerant implants, *i.e.*, fatigue-critical applications. In this work, Metal-Injection-Molded titanium alloys (Ti-MIM) containing either very high O-levels or very high O- and C-levels, were polluted-produced by using blended powders and changing the cleanliness of vacuum-sintering. Through investigations of high-cycle fatigue (HCF) behavior, the following can be concluded:

- Polluted-produced MIM β Ti-alloys can provide the HCF endurance limits beyond 600 MPa significantly higher than those of clean-produced MIM common α-β Ti-reference alloys.
- Its hierarchical dual-scale 3D "tent"-architecture of variously oriented α-platelets and slip/crack-unfavored micro-winding absolute grain boundaries, combined with proper solutes in Ti-matrix, can effectively retard fatigue small-crack presence.
- The microscale "tent"-architecture of α-platelets can compel the fatal/critical crack twists and tilts to effect cracking bifurcation and deflection, thereby triggering diverse crack closure mechanisms to hinder fatigue large-crack propagation.
- It endows MIM β Ti-alloys superior HCF performance exempt from high processing cleanliness that even a large number of oxygen and carbon does not facilitate crack initiation in "weak"-microstructural features/units.
- Two competing mechanisms of crack initiation could bring about a conditional fatigue duality only if a very high C-level is present. It can merely take place above a cyclic stress-threshold of ≈ 777 MPa where in addition to crack initiation at microscale pore α platelets also crack initiation at large pore TiC inclusions can occur.

Declaration of Competing Interest

The authors declare that they have no known competing financial interests or personal relationships that could have appeared to influence the work reported in this paper.

Acknowledgements

This research was supported by Helmholtz-Zentrum Hereon and Deutsches Elektronen-Synchrotron (DESY). The authors would like to thank Dr. A. Stark for the support in the in situ high-energy X-ray diffraction at the synchrotron beamline; P. Fischer and Dr. S. Yi for the assistance in electron backscatter diffraction; A. Dobernowsky, K. Erdmann, S. Riekehr, Dr. N. Kashaev, and C. Horstmann

for their technical help in metal-injection-molding, tensile testing, and fatigue testing; Prof. M. Yan for manuscript reviewing; and Dr. S. Gavras, T. Konkol for language polishing. In addition, Dr. P. Xu thanks to personnel and financial support from Helmholtz-Zentrum Hereon and Fraunhofer Institute IAPT.

Data availability

The raw/processed data required to reproduce these findings cannot be shared at this time as the data also forms part of an ongoing study.

Appendix A. Supplementary data

Supplementary data to this article can be found online at https://doi.org/10.1016/j.matdes.2021.110141.

References

[1] F.H. Froes, D. Eylon, Powder metallurgy of titanium alloys, Int. Mater. Rev. 35 (1) (1990) 162–184, https://doi.org/10.1179/095066090790323984.
[2] D.F. Heaney, Handbook of metal injection molding, Woodhead Publishing, Philadelphia, PA, 2012.
[3] R. German, Progress in titanium metal powder injection molding, Materials 6 (8) (2013) 3641–3662, https://doi.org/10.3390/ma6083641.
[4] P. Xu, F. Pyczak, M. Yan, W. Limberg, R. Willumeit-Römer, T. Ebel, Tensile toughening of powder-injection-molded β Ti-Nb-Zr biomaterials by adjusting TiC particle distribution from aligned to dispersed pattern, Appl. Mater. Today 19 (2020), https://doi.org/10.1016/j.apmt.2020.100630 100630.
[5] C.H. Turner, D.B. Burr, Basic biomechanical measurements of bone: A tutorial, Bone 14 (4) (1993) 595–608, https://doi.org/10.1016/8756-3282(93)90081-K.
[6] M. Geetha, A.K. Singh, R. Asokamani, A.K. Gogia, Ti based biomaterials, the ultimate choice for orthopaedic implants – A review, Prog. Mater. Sci. 54 (3) (2009) 397–425, https://doi.org/10.1016/j.pmatsci.2008.06.004.
[7] A. Biesiekierski, J. Wang, M.-A.-H. Gepreel, C. Wen, A new look at biomedical Ti-based shape memory alloys, Acta Biomater. 8 (5) (2012) 1661–1669, https://doi.org/10.1016/j.actbio.2012.01.018.
[8] S.J. Li, T.C. Cui, Y.L. Hao, R. Yang, Fatigue properties of a metastable β-type titanium alloy with reversible phase transformation, Acta Biomater. 4 (2) (2008) 305–317, https://doi.org/10.1016/j.actbio.2007.09.009.
[9] T. Ebel, O. Milagres Ferri, W. Limberg, M. Oehring, F. Pyczak, F.P. Schimansky, Metal injection moulding of titanium and titanium-aluminides, Key Eng. Mater. 520 (2012) 153–160, https://doi.org/10.4028/www.scientific.net/KEM.520.153.
[10] M. Yan, W. Xu, M.S. Dargusch, H.P. Tang, M. Brandt, M. Qian, Review of effect of oxygen on room temperature ductility of titanium and titanium alloys, Powder Metall. 57 (4) (2014) 251–257, https://doi.org/10.1179/1743290114Y.0000000108.
[11] T. Ebel, T. Beißig, S. Ebner, X. Luo, A.B. Nagaram, D. Zhao, Reduction of the embrittlement effect of binder contamination in MIM processing of Ti alloys, Powder Metall. 60 (3) (2017) 157–166, https://doi.org/10.1080/00325899.2017.1291085.
[12] F.C. Campbell, Fatigue and Fracture: Understanding the Basics, ASM International, Materials Park, OH, 2012.
[13] U.S.A.F.S.A. Board, Report of the AdHoc committee on air force aircraft jet engine manufacturing and SAF/AQQS, The pentagon, Washington, DC, 1992.
[14] C.-W. Lin, C.-P. Ju, J.-H. Chern Lin, A comparison of the fatigue behavior of cast Ti–7.5Mo with c.p. titanium, Ti–6Al–4V and Ti–13Nb–13Zr alloys, Biomaterials 26 (16) (2005) 2899–2907, https://doi.org/10.1016/j.biomaterials.2004.09.007.
[15] R.M. German, Titanium sintering science: A review of atomic events during densification, Int. J. Refract. Met. Hard Mater. 89 (2020) 105214, https://doi.org/10.1016/j.ijrmhm.2020.105214.
[16] R. Nalla, R. Ritchie, B. Boyce, J. Campbell, J. Peters, Influence of microstructure on high-cycle fatigue of Ti-6Al-4V: Bimodal vs. lamellar structures, Metall. Mater. Trans. A 33 (3) (2002) 899–918, https://doi.org/10.1007/s11661-002-0160-z.
[17] S. Suresh, R.O. Ritchie, Propagation of short fatigue cracks, Int. Mater. Rev. 29 (1) (1984) 445–475, https://doi.org/10.1179/imtr.1984.29.1.445.
[18] M. Peters, A. Gysler, G. Lütjering, Influence of texture on fatigue properties of Ti-6Al-4V, Metall. Mater. Trans. A 15 (8) (1984) 1597–1605, https://doi.org/10.1007/BF02657799.
[19] G. Lütjering, J.C. Williams, Titanium, Springer Science & Business Media, Berlin, Germany, 2007.
[20] O.M. Ferri, T. Ebel, R. Bormann, High cycle fatigue behaviour of Ti–6Al–4V fabricated by metal injection moulding technology, Mater. Sci. Eng. A 504 (1) (2009) 107–113, https://doi.org/10.1016/j.msea.2008.10.039.
[21] A.A. Hidalgo, T. Ebel, F. Pyczak, W. Limberg, E. Carreño-Morelli, R. Frykholm, B. Brash, Fundamental Understanding of the Influence of Oxygen on the Fatigue behaviour of Ti-6Al-7Nb Alloys, World PM2016 Congress & Exhibition, European Powder Metallurgy Association, Hamburg, Germany, 2016.
[22] O.M. Ferri, T. Ebel, R. Bormann, Influence of surface quality and porosity on fatigue behaviour of Ti–6Al–4V components processed by MIM, Mater. Sci. Eng. A 527 (7) (2010) 1800–1805, https://doi.org/10.1016/j.msea.2009.11.007.
[23] J.J. Kruzic, J.P. Campbell, R.O. Ritchie, On the fatigue behavior of γ-based titanium aluminides: role of small cracks, Acta Mater. 47 (3) (1999) 801–816, https://doi.org/10.1016/S1359-6454(98)00409-1.
[24] C. Leyens, M. Peters, Titanium and Titanium Alloys: Fundamentals and Applications, Wiley-VCH, Weinheim, Germany, 2003.
[25] D. Qiu, R. Shi, D. Zhang, W. Lu, Y. Wang, Variant selection by dislocations during α precipitation in α/β titanium alloys, Acta Mater. 88 (2015) 218–231, https://doi.org/10.1016/j.actamat.2014.12.044.
[26] R.O. Ritchie, J. Lankford, Small fatigue cracks: A statement of the problem and potential solutions, Mater. Sci. Eng. 84 (1986) 11–16, https://doi.org/10.1016/0025-5416(86)90217-X.
[27] T. Zhai, A.J. Wilkinson, J.W. Martin, A crystallographic mechanism for fatigue crack propagation through grain boundaries, Acta Mater. 48 (20) (2000) 4917–4927, https://doi.org/10.1016/S1359-6454(00)00214-7.
[28] J. Lindemann, C. Buque, F. Appel, Effect of shot peening on fatigue performance of a lamellar titanium aluminide alloy, Acta Mater. 54 (4) (2006) 1155–1164, https://doi.org/10.1016/j.actamat.2005.10.043.
[29] Z.Z. Fang, J.D. Paramore, P. Sun, K.S.R. Chandran, Y. Zhang, Y. Xia, F. Cao, M. Koopman, M. Free, Powder metallurgy of titanium – past, present, and future, Int. Mater. Rev. 63 (7) (2018) 407–459, https://doi.org/10.1080/09506608.2017.1366003.
[30] P. Xu, F. Pyczak, M. Yan, F. Kong, T. Ebel, Impacts of yttrium on microstructure and tensile properties of biomedical β Ti-Nb-Zr fabricated by metal injection molding, Mater. Sci. Eng. A 792 (2020), https://doi.org/10.1016/j.msea.2020.139816 139816.
[31] F. Cao, K.S.R. Chandran, P. Kumar, New approach to achieve high strength powder metallurgy Ti-6Al-4V alloy through accelerated sintering at β-transus temperature and hydrogenation-dehydrogenation treatment, Scripta Mater. 130 (2017) 22–26, https://doi.org/10.1016/j.scriptamat.2016.11.005.
[32] M. Abdel-Hady, K. Hinoshita, M. Morinaga, General approach to phase stability and elastic properties of β-type Ti-alloys using electronic parameters, Scripta Mater. 55 (5) (2006) 477–480, https://doi.org/10.1016/j.scriptamat.2006.04.022.
[33] D. Zhao, K. Chang, T. Ebel, H. Nie, R. Willumeit, F. Pyczak, Sintering behavior and mechanical properties of a metal injection molded Ti–Nb binary alloy as biomaterial, J. Alloys Compd. 640 (2015) 393–400, https://doi.org/10.1016/j.jallcom.2015.04.039.
[34] M. Yan, S. Luo, G. Schaffer, M. Qian, Impurity (Fe, Cl, and P)-induced grain boundary and secondary phases in commercially pure titanium (CP-Ti), Metall. Mater. Trans. A 44 (8) (2013) 3961–3969, https://doi.org/10.1007/s11661-013-1720-0.
[35] M. Yan, M. Qian, C. Kong, M.S. Dargusch, Impacts of trace carbon on the microstructure of as-sintered biomedical Ti–15Mo alloy and reassessment of the maximum carbon limit, Acta Biomater. 10 (2) (2014) 1014–1023, https://doi.org/10.1016/j.actbio.2013.10.034.
[36] D. Bhattacharyya, G.B. Viswanathan, H.L. Fraser, Crystallographic and morphological relationships between β phase and the Widmanstätten and allotriomorphic α phase at special β grain boundaries in an α/β titanium alloy, Acta Mater. 55 (20) (2007) 6765–6778, https://doi.org/10.1016/j.actamat.2007.08.029.
[37] S.M.C. van Bohemen, A. Kamp, R.H. Petrov, L.A.I. Kestens, J. Sietsma, Nucleation and variant selection of secondary α plates in a β Ti alloy, Acta Mater. 56 (20) (2008) 5907–5914, https://doi.org/10.1016/j.actamat.2008.08.016.
[38] D. Bhattacharyya, G.B. Viswanathan, R. Denkenberger, D. Furrer, H.L. Fraser, The role of crystallographic and geometrical relationships between α and β phases in an α/β titanium alloy, Acta Mater. 51 (16) (2003) 4679–4691, https://doi.org/10.1016/S1359-6454(03)00179-4.
[39] M. Niinomi, M. Nakai, J. Hieda, Development of new metallic alloys for biomedical applications, Acta Biomater. 8 (11) (2012) 3888–3903, https://doi.org/10.1016/j.actbio.2012.06.037.
[40] Q. Yu, L. Qi, T. Tsuru, R. Traylor, D. Rugg, J.W. Morris, M. Asta, D.C. Chrzan, A.M. Minor, Origin of dramatic oxygen solute strengthening effect in titanium, Science 347 (6222) (2015) 635, https://doi.org/10.1126/science.1260485.
[41] Q.C. Jiang, X.L. Li, H.Y. Wang, Fabrication of TiC particulate reinforced magnesium matrix composites, Scripta Mater. 48 (6) (2003) 713–717, https://doi.org/10.1016/S1359-6462(02)00551-1.
[42] P. Wanjara, R.A.L. Drew, J. Root, S. Yue, Evidence for stable stoichiometric Ti2C at the interface in TiC particulate reinforced Ti alloy composites, Acta Mater. 48 (7) (2000) 1443–1450, https://doi.org/10.1016/S1359-6454(99)00453-X.
[43] M.R. Bache, W.J. Evans, M. McElhone, The effects of environment and internal oxygen on fatigue crack propagation in ti-6al-4v, Mater. Sci. Eng. A 234–236 (1997) 918–922, https://doi.org/10.1016/S0921-5093(97)00402-4.
[44] A.A. Hidalgo, T. Ebel, W. Limberg, F. Pyczak, Influence of oxygen on the fatigue behaviour of Ti-6Al-7Nb alloy, Key Eng. Mater. 704 (2016) 44–52, https://doi.org/10.4028/www.scientific.net/KEM.704.44.
[45] C. Leinenbach, D. Eifler, Influence of oxidation treatment on fatigue and fatigue-induced damage of commercially pure titanium, Acta Biomater. 5 (7) (2009) 2810–2819, https://doi.org/10.1016/j.actbio.2009.03.029.
[46] D.P. Satko, J.B. Shaffer, J.S. Tiley, S.L. Semiatin, A.L. Pilchak, S.R. Kalidindi, Y. Kosaka, M.G. Glavicic, A.A. Salem, Effect of microstructure on oxygen rich layer evolution and its impact on fatigue life during high-temperature application of

α/β titanium, Acta Mater. 107 (2016) 377–389, https://doi.org/10.1016/j.actamat.2016.01.058.
[47] H. Liu, M. Niinomi, M. Nakai, S. Obara, H. Fujii, Improved fatigue properties with maintaining low Young's modulus achieved in biomedical beta-type titanium alloy by oxygen addition, Mater. Sci. Eng. A 704 (2017) 10–17, https://doi.org/10.1016/j.msea.2017.07.078.
[48] M. Long, R. Crooks, H.J. Rack, High-cycle fatigue performance of solution-treated metastable-β titanium alloys, Acta Mater. 47 (2) (1999) 661–669, https://doi.org/10.1016/S1359-6454(98)00343-7.
[49] K. Cho, M. Niinomi, M. Nakai, J. Hieda, R. Kanekiyo, Improvement of Tensile and Fatigue Properties of β-Titanium Alloy while Maintaining Low Young's Modulus through Grain Refinement and Oxygen Addition, Mater. Trans. 54 (10) (2013) 2000–2006, https://doi.org/10.2320/matertrans.M2013151.
[50] G. Yoder, F. Froes, D. Eylon, Effect of microstructure, strength, and oxygen content on fatigue crack growth rate of Ti-4.5Al-5.0Mo-1.5Cr, Metall. Trans. A 15 (1) (1984) 183–197, https://doi.org/10.1007/BF02644400.
[51] F. Briffod, A. Bleuset, T. Shiraiwa, M. Enoki, Effect of crystallographic orientation and geometrical compatibility on fatigue crack initiation and propagation in rolled Ti-6Al-4V alloy, Acta Mater. 177 (2019) 56–67, https://doi.org/10.1016/j.actamat.2019.07.025.
[52] R.O. Ritchie, Mechanisms of fatigue-crack propagation in ductile and brittle solids, Int. J. Fract. 100 (1) (1999) 55–83, https://doi.org/10.1023/A:1018655917051.
[53] A.N. May, A Model of Metal Fatigue, Nature 185 (4709) (1960) 303–304, https://doi.org/10.1038/185303a0.
[54] D. Davidson, K. Chan, R. McClung, S. Hudak, Small Fatigue Cracks, in: I. Milne, R.O. Ritchie, B. Karihaloo (Eds.), Comprehensive Structural Integrity, Elsevier Pergamon, Oxford, UK, 2003, pp. 129–164.
[55] N.F. Mott, Bakerian Lecture: Dislocations, plastic flow and creep, Proceedings of the Royal Society A: Mathematical, Physical and Engineering Sciences 220 (1140) (1953) 1–14, https://doi.org/10.1098/rspa.1953.0167.
[56] A.N. Stroh, N.F. Mott, The formation of cracks as a result of plastic flow, Proceedings of the Royal Society A: Mathematical, Physical and Engineering Sciences 223 (1154) (1954) 404–414, https://doi.org/10.1098/rspa.1954.0124.
[57] P. Neumann, Coarse slip model of fatigue, Acta Metall. 17 (9) (1969) 1219–1225, https://doi.org/10.1016/0001-6160(69)90099-6.
[58] C.C. Wojcik, K.S. Chan, D.A. Koss, Stage I fatigue crack propagation in a titanium alloy, Acta Metall. 36 (5) (1988) 1261–1270, https://doi.org/10.1016/0001-6160(88)90278-7.
[59] P.C. Paris, G.C. Sih, Stress Analysis of Cracks, in: W.F.B. Jr (Ed.), Fracture Toughness Testing and its Applications, American Society for Testing and Materials, Philadelphia, PA, 1965, pp. 30–83.
[60] G. Qian, Z. Jian, X. Pan, F. Berto, In-situ investigation on fatigue behaviors of Ti-6Al-4V manufactured by selective laser melting, Int. J. Fatigue 133 (2020), https://doi.org/10.1016/j.ijfatigue.2019.105424 105424.
[61] Y. Gao, J.S. Stölken, M. Kumar, R.O. Ritchie, High-cycle fatigue of nickel-base superalloy René 104 (ME3): Interaction of microstructurally small cracks with grain boundaries of known character, Acta Mater. 55 (9) (2007) 3155–3167, https://doi.org/10.1016/j.actamat.2007.01.033.
[62] R.O. Ritchie, The conflicts between strength and toughness, Nat. Mater. 10 (11) (2011) 817–822, https://doi.org/10.1038/nmat3115.
[63] D.J. Rowenhorst, A.C. Lewis, G. Spanos, Three-dimensional analysis of grain topology and interface curvature in a β-titanium alloy, Acta Mater. 58 (16) (2010) 5511–5519, https://doi.org/10.1016/j.actamat.2010.06.030.
[64] E. Hryha, L. Nyborg, A. Malas, S. Wiberg, S. Berg, Carbon control in PM sintering: industrial applications and experience, Powder Metall. 56 (1) (2013) 5–10, https://doi.org/10.1179/0032589912Z.00000000085.
[65] K.S.R. Chandran, Duality of fatigue failures of materials caused by Poisson defect statistics of competing failure modes, Nat. Mater. 4 (4) (2005) 303–308, https://doi.org/10.1038/nmat1351.
[66] K.S. Ravi Chandran, P. Chang, G.T. Cashman, Competing failure modes and complex S–N curves in fatigue of structural materials, Int. J. Fatigue 32 (3) (2010) 482–491, https://doi.org/10.1016/j.ijfatigue.2009.08.004.